

Characteristics and Electrochemical Performances of Nitrogen-doped Graphene Prepared using different carbon and nitrogen sources as Anode for Lithium Ion Batteries

Hong Liu, Yichen Deng, Jinxiang Mao, Minmin Chen, Jinxia Hu, Zhicheng Ju, Zheng Xing and Xichuan Cao*

Department of Energy Materials and Devices, School of Materials and Physics, China University of Mining and Technology, Xu Zhou 221000, China

*E-mail: xichuancao@cumt.edu.cn

Received: 4 November 2020 / Accepted: 24 January 2021 / Published: 28 February 2021

Nitrogen-doped graphene (NG) materials were successfully synthesized in one step by the restricted template method. Specifically, the use of different nitrogen sources and carbon sources makes the content of various nitrogen doping structures in NGs different and yields a higher nitrogen doping amount. In the lithium insertion process, nitrogen doping provides more active sites, which effectively improve the specific capacity. As anodes for lithium-ion batteries (LIBs), NGs exhibit excellent electrochemical performance with high reversible specific capacity, good cycle stability, and excellent rate performance.

Keywords: Nitrogen-doped Graphene, Anode material, Lithium-ion batteries

1. INTRODUCTION

Graphene is a multifunctional nanomaterial with a single layer of carbon atoms bonded in a hexagonal lattice [1]. Since it was first prepared through the micromechanical peeling method by Geim et al. in 2004 [2], graphene has been established as one of the most attractive substances in the field of energy materials. As a research hot spot for lithium-ion battery (LIB) anode materials, graphene has an obvious charging and discharging platform and a low platform potential (0.01~0.2 V vs Li), which provide a high and stable working voltage [3]. However, the specific capacity of graphite lithium intercalation is high; its lithium intercalation compound can reach its theoretical composition as LiC_6 , and the corresponding theoretical specific capacity is merely $372 \text{ mAh}\cdot\text{g}^{-1}$ [4]. To improve the application issues of graphene and give full play to its excellent properties, graphene with various morphologies has been designed and explored in recent years, including two-dimensional graphene nanosheets (GNSs) [5-7], one-dimensional graphene nanoribbons (GNRs) [8-9], and zero-dimensional

graphene quantum dots (GQDs) [10-13]. Apart from morphological control, doping is another important method for enhancing the properties of graphene [14-15]. Generally, there are two main approaches to graphene doping. The first point is to introduce adsorbable substances, including inorganic nonmetal oxides [16], metals and metal oxides [17-19]. In addition, organic molecules [20] can be absorbed onto the surfaces of graphene materials. The other is substitution, in which heteroatoms such as nitrogen, phosphorus and boron can substitute for the original carbon atoms in the carbon lattice [21-24].

In addition, graphene doping with nitrogen atoms is an effective way to improve the performance of anode electrode materials in LIB systems. Several studies on nitrogen atom-doped graphene (NG) have been mentioned. First, nitrogen atoms are doped into graphene utilizing direct synthesis techniques such as chemical vapor deposition (CVD) and solvothermal and arc-discharge methods [25-26]. Postprocessing involves heat, plasma and nitrogenous chemical treatments [27-28]. These nitrogen atoms usually gave the carbon materials three different chemical structures classified as graphitic N, pyridinic N, and pyrrolic N atoms (Figure 1) [29] when they were successfully doped into the carbon lattice. Nitrogen doping can open the energy band gap, adjust the conductivity type, change the electronic structure and increase the free carrier density of graphene; thus, nitrogen doping could efficiently improve the conductivity and stability and greatly enhance anode performance for LIBs [30].

Previously, several studies dealing with nitrogen-doped graphene as an anode have been reported [31-32]. To achieve nitrogen-doped graphite, Huang et al. used hydrazine hydrate as a reductant to reduce graphene oxide through a solvent reduction method. The successfully synthesized nitrogen-doped graphite complexes used as electrode materials for LiB exhibited outstanding electrochemical performance [33]. Chen et al. prepared a silicon flake/nitrogen-doped graphene (Si/NG) composite via an in situ strategy. This reveals that Si/NG production possesses a hierarchical porous architecture, large specific surface area and lamellar morphology. Similarly, this synthesized Si/NG production used as electrode materials also endowed outstanding electrochemical performance [34]. In this article, an NG material synthesized by a simple method is presented, and its electrochemical performance is characterized.

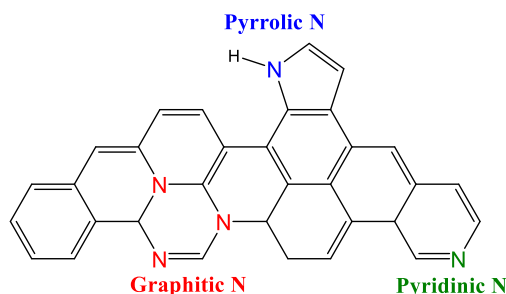


Figure 1. Schematic diagram of the bond structure of nitrogen-doped graphene [29].

Herein, a restricted template method was utilized to prepare NG materials in one step. A series

of NG materials were synthesized with melamine, urea, and dicyandiamide as the nitrogen sources and glucose, methyl cellulose, and sucrose as the carbon sources. The chemical structures and morphology of the synthesized materials were characterized by XRD, FT-IR, XPS, SEM and TEM technologies. All these materials have twisted stacked sheet morphologies with pore structures, and nitrogen atoms are doped successfully into NG materials. As anodes for LIBs, compared to pure graphite materials, these NG materials also exhibit better cycle performance (the reversible specific capacity is 780 mAh·g⁻¹ at a current density of 100 mA·g⁻¹ after 100 cycles) and rate performance (331.8 mAh·g⁻¹ at 5.0 A·g⁻¹).

2. EXPERIMENTAL SECTION

2.1. Chemicals and reagents

The deionized water used in all the experiments was produced by EPED-E2-20TJ ultrapure water equipment (Nanjing, China). Melamine (99%), urea (99%), dicyandiamide (99%), and anhydrous ethanol were purchased from Sinopharm Chemical Reagent Co., Ltd. (Shanghai, China). Glucose, methyl cellulose, and sucrose were purchased from Aladdin Industrial Co., Ltd. (Shanghai, China). All chemicals and solvents were of analytical grade and used without further purification.

2.2. Synthesis of Nitrogen-doped Graphene

Nitrogen-doped graphene (NG) was synthesized in one step via a restricted template method. Typically, 10 g of melamine and 1 g of glucose were weighed into a stainless-steel ball mill tank with a mass ratio of 10:1, followed by the addition of an equal volume of anhydrous ethanol. After ball milling for 6 hours, the precursor mixture was dried at 60°C for 12 hours in an oven. Subsequently, the completely dried precursor was heat-treated under argon in a tube furnace. The heating step was as follows: first, the sample was heated for 4 hours at 580°C with a heating rate of 2°C·min⁻¹, then increased to 800°C with the same heating rate, and that temperature was held for another 2 hours. After cooling to room temperature in the furnace, the synthesized NG materials (NGS1) were ground, washed with alcohol and dried. Analogously, the products (NGS2, NGS3, NGS4, NGS5) were prepared from other nitrogen and carbon sources (Table 1) with the same processing method.

Table 1. NG products with different nitrogen and carbon sources

Sample ID	Nitrogen sources	Carbon sources
NGS1	Melamine	Glucose
NGS2	Urea	Glucose
NGS3	Dicyandiamide	Glucose
NGS4	Melamine	Methyl cellulose
NGS5	Melamine	Sucrose

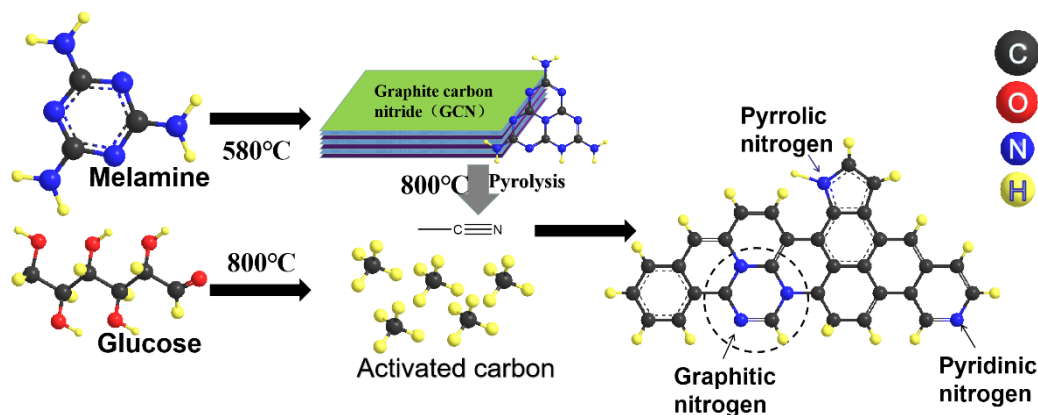


Figure 2. Schematic diagram of the synthesis mechanism of NGS1.

The reaction mechanism diagram using NGS1 as an example is shown in Figure 2. The restricted template method was used in the synthesis of nitrogen-doped graphite materials. During the first stage of heat treatment at 580°C for 4 hours, the nitrogen source was pyrolyzed and formed a layered structure of graphitized carbon-nitrogen compound templates. The aromatic carbon atoms of the carbon source were attached between the abovementioned graphitized carbon-nitrogen compound interlayer gaps [35]. In the second stage of heating at 800°C for 2 hours, the graphitized carbon-nitrogen compound template was removed under high temperature. A single-layer and multilayer graphite layer stack structure of NG was formed. In the restricted template method, the nitrogen source will undergo pyrolysis at 580 °C to form graphite carbon nitride (GCN). In the further heating process, it will continue to decompose to cyanide. Therefore, activated carbon atoms can react with cyanide to achieve nitrogen doping under high temperature conditions [36].

2.3. Characterization method

The samples were characterized by scanning electron microscopy (JSM-6700F), transmission electron microscopy (Hitachi HT-7700), X-ray powder diffraction (PANalytical X'Pert PRO), Raman spectroscopy (Thermo Scientific DXR) and X-ray photoelectron spectroscopy (VG Escalab Mark 2). Specific device information and details of the measurements can be found in our previous work [35].

2.4. Electrochemical measurements

Synthesized NGs were used as the active material for two-electrode 2025 coin-type battery assemblies. The battery charge and discharge test was performed using the LAND CT-2001A (Wuhan) system. Electrochemical impedance spectroscopy (EIS) and cyclic voltammetry (CV) measurements were performed with a CHI 1140A system. The battery assembly process and related test details are consistent with our previous work [35].

3. RESULTS AND DISCUSSION

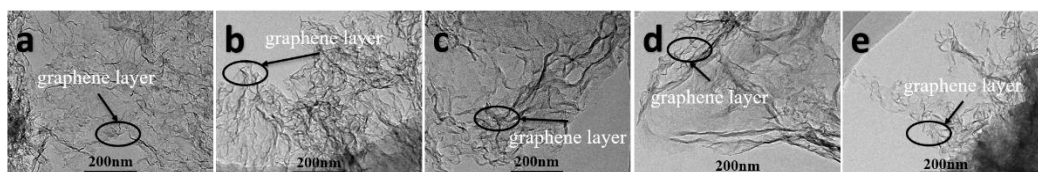


Figure 3. TEM images of (a) NGS1, (b) NGS2, (c) NGS3, (d) NGS4, and (e) NGS5.

As shown in the TEM results (Figure 3), the NG morphologies are not significantly different. It was obvious that the materials were composed of twisted stacked graphene sheets and had certain edge bending and macropore structures. Correspondingly, the SEM images in Figure S1 also displayed the same result. These macropores and the layered curved structure increased the specific surface area, thereby enhancing the active sites for lithium ions. NGs were formed by single-layer and multilayer graphite layers, with the edges of the carbon nanosheets curled. The cause of this structure is mainly the doping of nitrogen atoms, so many lattice defects are formed in the carbon nanosheet layer, which causes uneven stress on the surface of the carbon nanosheet [37]. Therefore, a curled morphological structure appears. In addition, lattice defects also lead to a weakening of the bonding force between the sheets, thereby increasing the spacing between the stacked graphite sheets, which is beneficial to reducing the number of stacked layers and further improving the overall material confusion [38]. The twisted staggered structure of the sheet layer provides a considerable number of holes in the material. These holes further increase the specific surface area of the material and shorten the solid-state transmission distance of Li^+ , which is beneficial for improving its specific capacity and rate performance when used as an anode electrode material for LIBs [39]. In addition, according to the SEM and TEM results of NGs, when different nitrogen and carbon sources are used, the microstructure and morphology of the synthesized NG have not changed, indicating that the method has more options for nitrogen and carbon sources. This result also shows the flexibility of the synthesis method used.

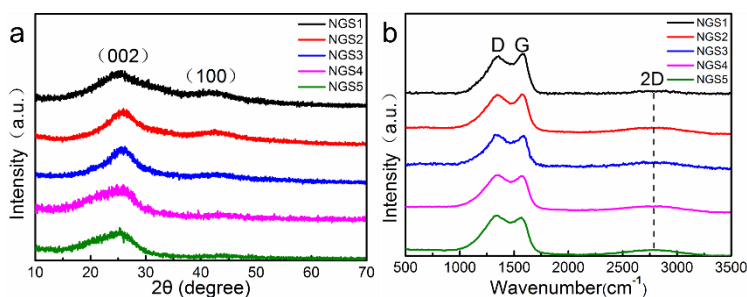


Figure 4. (a) XRD patterns and (b) Raman spectra of NGs.

The crystalline structures of the as-synthesized NGs were investigated by XRD. As shown in Figure 4a, diffraction peaks at 2θ of 26° (002) and 43° (100) can be observed, which correspond to the

diffraction peaks of graphitic carbon and amorphous carbon. The diffraction curves of the five NGs are basically the same as those in Figure 4a, indicating that the different nitrogen sources and carbon sources used did not change the structure of the synthesized NGs [40]. In addition, through the Bragg equation ($2d\sin\theta = n\lambda$), the graphene structure interplane distances of NGS1, NGS2, NGS3, NGS4, and NGS5 are 3.36 nm, 3.43 nm, 3.45 nm, 3.40 nm, and 3.49 nm, respectively. The relatively broad diffraction peaks also indicate that the NGs have uneven graphite structure layer spacing, that is, they have a high overall material confusion. The large interlayer spacing also provides the possibility of recombination with other material structures [41].

Characterization by laser confocal Raman spectroscopy can explore the degree of graphitization of carbon in the prepared graphene material. The results in Figure 4b show two characteristic peaks at 1345 cm^{-1} and 1570 cm^{-1} , which correspond to the D and G peaks, respectively. The D peak (defect peak) is mainly caused by lattice defects of carbon atoms, disordered carbon structure, and unsaturated carbon atoms at the edges. The higher the peak is, the more defects there are in the carbon atom crystal. The G peak is the graphite peak [42,43], corresponding to the in-plane stretching vibration peak of sp^2 hybridized carbon atoms, representing the formation of the graphite carbon structure. The relative intensity ratio I_D/I_G of the D peak to the G peak represents the degree of disorder of the five NGs. The calculation of Raman spectrum peak data shows that the I_D/I_G values of samples NGS1, NGS2, and NGS3 with glucose as the carbon source and different nitrogen sources are 0.96, 1.01, and 1.04, respectively. The I_D/I_G values of NGS1, NGS4 and NGS5 with melamine as the nitrogen source and different carbon sources were 0.96, 1.02 and 0.97, respectively. That is, there are more defects in NGS3 and NGS4 of the two groups of samples. The increase in such defects is beneficial to providing more lithium storage active sites and increasing their reversible specific capacity. In addition, there are obvious 2D peaks in all five samples, which are located near 2800 cm^{-1} . The 2D peak mainly comes from the second-order form of regional boundary phonons, which characterizes the interlayer stacking of carbon atoms in graphite samples [35]. The appearance of 2D peaks indicates that there is a certain graphene layer in all five samples, and its broad 2D peak shows that the synthesized material has a higher overall degree of disorder, and this result is also consistent with the XRD and TEM results.

Table 2. The proportion of surface atoms of NGs

Sample ID	C1s	N1s	O1s
NGS1	77.92	12.68	9.4
NGS2	78.2	17.25	4.55
NGS3	75.51	19.59	4.89
NGS4	76.99	16.34	5.01
NGS5	84.54	11.58	3.35

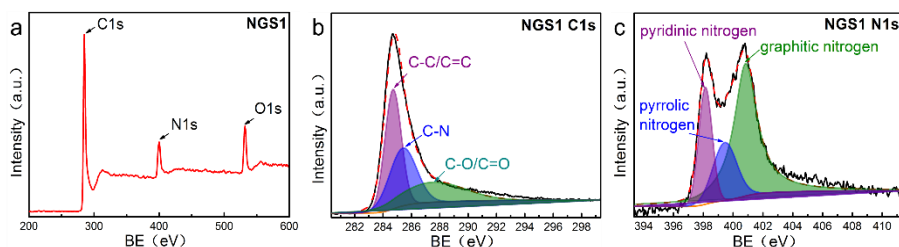


Figure 5. (a) XPS full spectrum, (b) C1s XPS and (c) N1s XPS spectra of NGS1.

Characterization of NGs by XPS can further study the valence state and content of each element in the material. Table 2 is the proportion of the elements on the exterior of the NGs, which revealed that the facial nitrogen doping amounts of the NGS1, NGS2, NGS3, NGS4 and NGS5 samples are 12.68 at.%, 17.25 at.%, 19.59 at.%, 16.34 at.%, and 11.58 at.%, respectively, indicating that the sample is successfully doped with nitrogen and has a higher doping amount. The higher oxygen content in the sample is mainly derived from the oxygen-containing functional groups of the sample. The full XPS spectrum of sample NGS1 (Figure 5a) illustrated that there are obvious C1s, N1s and O1s characteristic peaks. The C1s narrow-sweep energy spectrum peak splitting results (Figure 5b) show that the strongest peak at 284.7 eV corresponds to the sp^2 hybridized C-C/C=C structure or graphite-structured C-N. The subpeak at 285.4 eV corresponds to the sp^2 hybridized C-N structure, and the subpeak at 287.5 eV corresponds to the sp^3 hybridized C-O/C=O bond structure [44]. The peak-splitting treatment of the N1s narrow-sweep energy spectrum (Figure 5c) shows that the doping form of nitrogen is mainly divided into the pyridine nitrogen (398.1 eV), pyrrole nitrogen (399.2 eV) and graphite nitrogen (400.5 eV), of which pyridine type and pyrrole nitrogen doping will damage the carbon ring structure of graphite [45]. Therefore, compared with graphite-type nitrogen doping, these two doping forms can cause more lattice defects and improve the material surface activity and roughness, which is more conducive to the improvement of its lithium storage performance and enhances the compounding ability of the material with other materials [46]. Further comparisons of peak area calculations showed that the contents of pyridine nitrogen, pyrrole nitrogen and graphite structure nitrogen in NGS1 are 25.8%, 23.3% and 50.9%, respectively. Comparison with the NGS2 and NGS3 XPS results in Figure S2a-f shows that NGS1 has a higher content of pyrrole nitrogen and graphite nitrogen structures and NGS3 has a higher content of pyridine nitrogen structures. In addition, comparing the XPS results of NGS1, NGS4 and NGS5 (Figure S2g-l), the contents of pyrrole nitrogen and graphite nitrogen structures in NGS1 and NGS5 are higher, while the content of pyridine nitrogen structures is less than that in NGS4. The XPS comparison results in Figure 5 and Figure S2 of the materials show that, when different carbon or nitrogen sources are selected, nitrogen-doped graphene materials with higher nitrogen doping can be successfully synthesized, and the difference in the structures between the nitrogen and carbon sources will have a certain influence on the of nitrogen-doped structures.

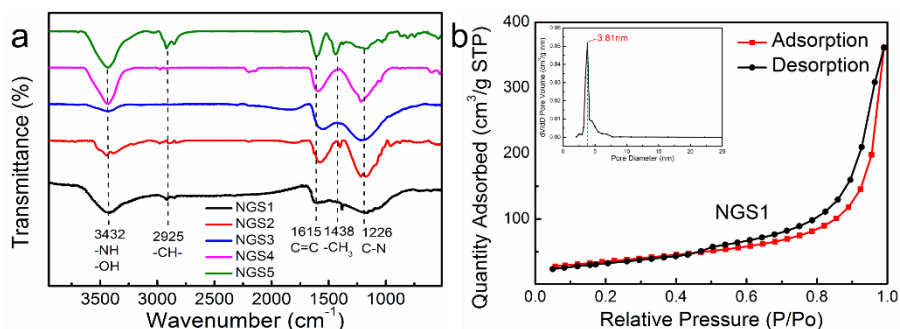


Figure 6. (a) FT-IR spectra of NGS1, NGS2, NGS3, NGS4 and NGS5. (b) Nitrogen adsorption–desorption and pore size distribution curve of NGS1.

Figure 6a is a comparison of the Fourier-transform infrared (FT-IR) absorption spectra of these five different nitrogen-doped graphene materials. The figure shows that the materials all have relatively obvious peaks near 2925, 1615 and 1226 cm^{-1} . These three peaks correspond to CH_2 , $\text{C}=\text{C}$ and $\text{C}-\text{N}$ stretching vibrations [47]. The strong and broad peaks near 3432 cm^{-1} correspond to the stretching vibrations of the $\text{O}-\text{H}$ and $\text{N}-\text{H}$ structures. The peak near 1438 cm^{-1} is due to the bending vibration of the CH_3 structure. The weaker peaks appearing near 2250 cm^{-1} mainly correspond to the $\text{C}\equiv\text{N}$ structure. Additionally, the peaks appearing in the range of 500 to 1000 cm^{-1} mainly correspond to the out-of-plane bending vibration of the $\text{C}-\text{H}$ structure and $\text{C}-\text{O}$ structure in different substituted structures of the benzene ring [48]. The FT-IR results also confirm the successful doping of nitrogen atoms in the materials.

Table 3. Related research on nitrogen-doped carbon materials as lithium-ion battery anodes

Sample ID	Methods	Nitrogen ratio (at. %)	Cycle number	Specific discharge capacity ($\text{mAh}\cdot\text{g}^{-1}$) ₁₎	Current density ($\text{mA}\cdot\text{g}^{-1}$)/Ref.
NGS1	Restricted template	12.68	100 300	780 310	100 (this work) 2000
NGA	Graphene oxide reduction	1.93	100	230	100 [16]
N-rGO I	Graphene oxide reduction	7.11	100	465	200 [48]
N-GNSPs	PECVD	7.5	3	423	100 [49]
BC-PANI_AC	Ammonium persulfate	-	200	438	372 [50]
	Carbonization				
NGA	Hydrothermal	3.26	150	143	372 [51]
C-700	Carbonization	2.54	500	450	200 [52]

The results in Figure 6b show that the hysteresis loop of NGS1 is a typical H4 type, which is mainly due to the synergy between the pore structure in the graphene layer and the gap caused by the stack. The pore size analysis results showed that NGS1 had numerous mesopores with diameters of 3.81 nm and some pores in the ranges of 2-3 nm and 4-7 nm in diameter. Furthermore, the Brunauer-Emmett-Teller (BET) method determined that NGS1 had a specific surface area of $124.69 \text{ m}^2 \cdot \text{g}^{-1}$ and a pore bulk of $0.55 \text{ cm}^3 \cdot \text{g}^{-1}$. NGS1 had a large specific surface area and pore volume. On one hand, this is due to the properties of the graphene material itself, and, on the other hand, it benefits from the large number of defects introduced by the doping of nitrogen atoms, that is, the pore and interstitial structure. This result was conducive to the transport of electrons and lithium ions in the electrode material, effectively increasing the interface area between the electrode material and the electrolyte and providing more active sites for lithium storage, thereby improving battery performance.

Compared with recent related studies, the NGs prepared by the restricted template method in this work are relatively simple, and the material has obviously obtained a higher nitrogen atom doping content, which is conducive to its performance as an anode. The comparison of battery capacity shows that, compared with graphite materials, nitrogen-doped carbon materials can obtain higher capacity. The NGS1 prepared in this work also exhibits a higher capacity. In addition, in this article, we discussed the performances of NG samples obtained by different nitrogen and carbon sources. In this method, the NG prepared using melamine and glucose shows a superior performance.

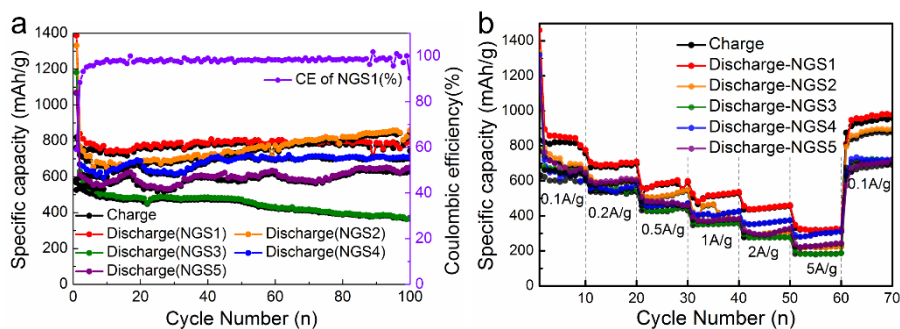


Figure 7. (a) Cycling performance of NGS1, NGS2, NGS3, NGS4 and NGS5 with a current density of $100 \text{ mA} \cdot \text{g}^{-1}$. (b) Rate performances of NGS1, NGS2, NGS3, NGS4 and NGS5 with various current densities.

The electrochemical properties of NGs were further explored for lithium batteries. Figure 7 shows the constant current charge-discharge curves and the rate performance test curves of NGs. The charge-discharge results in Figure 7a reveal that the capacity of NGS1 tends to be stable after the first cycle, and the coulombic efficiency remains above 98%. The capacity of the NGS1 electrode materials decreased from the 1st to the 10th cycle, then increased between the 10th and 20th cycles, finally stabilized after the 20th cycle and remained at $780 \text{ mAh} \cdot \text{g}^{-1}$ after the 100th cycle. The NGS2 electrode material showed a downward trend during the 1st to 15th cycle and then showed an upward trend. The main reason is that the charge-discharge reaction of the material during the cycle causes changes in its

material structure and nitrogen doping form, which increases the number of lithium storage active sites [53]. On the other hand, during the continuous cycle process, the compatibility between the electrolyte, the electrode, and the separator continues to increase, which increases the internal diffusion coefficient of the active material and improves the battery performance [54]. When 100 cycles are reached, the capacity of sample NGS2 can stabilize at $850.7 \text{ mAh}\cdot\text{g}^{-1}$, which is slightly higher than that of the first cycle, so NGS2 also has good lithium storage performance and cycle stability performance. The specific capacity of the NGS3 material continued to decrease during the cycle. After 100 cycles, the capacity decreased from an initial 567.5 to $366.2 \text{ mAh}\cdot\text{g}^{-1}$. That is, NG materials synthesized by glucose and melamine exhibited higher capacity and better cycle stability. The NGS4 and NGS5 electrode materials exhibited lower specific capacities than NGS1, which stabilized at $711 \text{ mAh}\cdot\text{g}^{-1}$ and $640 \text{ mAh}\cdot\text{g}^{-1}$ after 100 cycles and had a stable efficiency of more than 98%. When melamine is used as the nitrogen source, the cycle performance of a NG material using glucose as the carbon source is higher than for those using methyl cellulose and sucrose as the carbon source.

Figure 7b shows a comparison graph of the NG material's rate performances. The current density settings of the test are $0.1, 0.2, 0.5, 1, 2, 5$ and $0.1 \text{ A}\cdot\text{g}^{-1}$. The results in the figure show that, when the test current density continues to increase, the capacity of the NG material decreases. At a high current density of $5 \text{ A}\cdot\text{g}^{-1}$, the specific capacities of the NGS1-5 materials reached $331.8, 216.6, 184.8, 277.5,$ and $223.2 \text{ mAh}\cdot\text{g}^{-1}$, respectively. Compared with other NGs, NGS1 has a higher specific capacity at each current density. The reversible specific capacities increased to some extent relative to the initial specific capacity when the current density was restored to $0.1 \text{ A}\cdot\text{g}^{-1}$. The reason for this phenomenon is the large current density causing the microstructure of the electrode material to change and tending to form microscale and nanoscale features. A certain number of microporous structures were added, which led to the improvement of the specific surface area, therefore providing lithium storage with more active sites [55].

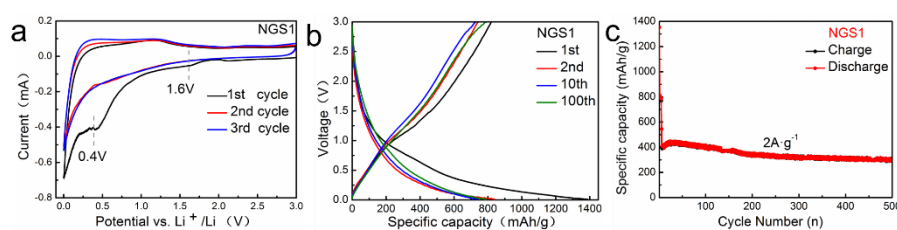


Figure 8. (a) CV curves of NGS1 at a scan rate of $0.2 \text{ mV}\cdot\text{s}^{-1}$ between 0.01 and 3.0 V versus Li^+/Li . (b) Discharge/charge curve of NGS1. (c) Cycle performance of NGS1 at a current density of $2 \text{ A}\cdot\text{g}^{-1}$.

The initial three cycles of CV curves of NGS1 are shown in Figure 8a. The voltage range set in the cyclic voltammetry test was 0.01 - 3.0 V and the sweep speed was set to $0.2 \text{ mV}\cdot\text{s}^{-1}$. The results illustrate that NGS1 displayed a clear reduction peak near 0.4 V in the 1st-cycle anode scan curve, corresponding to the formation process of the upper solid electrolyte interface (SEI) membrane [56]. Furthermore, it also has a weaker reduction peak at 1.6 V due to the irreversible reaction between the

oxygen-containing functional groups of the electrode material and the electrolyte. Compared with the CV results of the other four NGs in Figure S3, due to the difference in the types and contents of oxygen-containing groups, deviation of the reduction peak position also occurs. The reduction peak is also the main factor causing the formation of irreversible specific capacity in the first lap. Meanwhile, the described reduction peak began to disappear during the second cycle of scanning, which can indicate that its irreversible reaction was completed during the first cycle of discharge. The sharp reduction peaks of the materials in the range of less than 0.1 V was the Li^+ insertion process during the cycling process of the LIBs, which was also the main part of the capacity of the LIBs. The Li^+ extraction process corresponds to a broad oxidation peak near 0.25 V and 1.25 V.

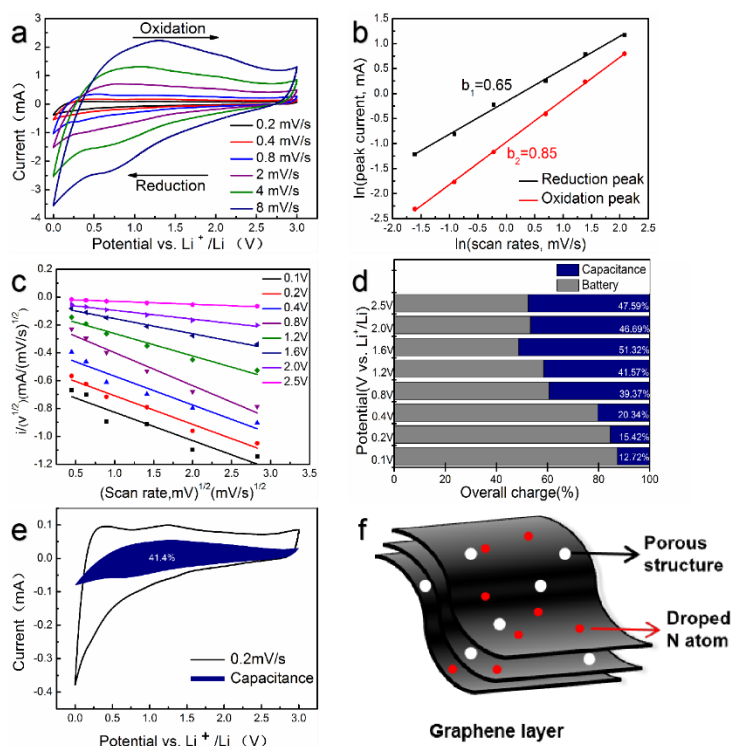


Figure 9. (a) Cyclic voltammetry test curves of NGS1 under different scanning speeds ($0.2\text{--}8\text{ mV}\cdot\text{s}^{-1}$). (b) Linear fitting graph under redox potential. (c) Linear fitting graph under different potentials. (d) Proportion of capacitance contribution at different potentials. (e) Cyclic voltammetry curve and capacitance contribution distribution at 0.2 mV/s . (f) Schematic of NGS1.

Figure 8b shows the NGS1 voltage plateaus during the battery cycle process of the 1st, 2nd, 10th, and 100th cycles. The initial discharge specific capacity of NGS1 is $1387.6\text{ mAh}\cdot\text{g}^{-1}$, and the premier charge specific capacity is $819.7\text{ mAh}\cdot\text{g}^{-1}$; that is, the first cycle coulombic efficiency is 59.07%. After the 100th cycle, the specific capacity reached $780\text{ mAh}\cdot\text{g}^{-1}$, while the theoretical specific capacity of commercial graphite was $372\text{ mAh}\cdot\text{g}^{-1}$. The results for NGS1 were relatively high, which was mainly due to the addition of nitrogen atoms forming an abundance of lattice defects and pore structures, and nitrogen atoms also increased the battery's ability to intercalate lithium. The irreversibility of the formation of oxygen-containing functional groups and the SEI membrane also

makes the material exhibit a larger irreversible capacity in the first cycle. There is no obvious voltage platform in the curves, which is consistent with the current research regarding graphite anode materials [57]. Otherwise, to further illustrate the battery cycle stability of NGS1 at a large current density, the electrode was first cycled five times at $100 \text{ mA}\cdot\text{g}^{-1}$, and then 500 charge and discharge cycles were performed at $2 \text{ A}\cdot\text{g}^{-1}$. The results are shown in Figure 8c. First, the initial specific capacity of the NGS1 electrode was $401.25 \text{ mAh}\cdot\text{g}^{-1}$, which gradually increased to $433 \text{ mAh}\cdot\text{g}^{-1}$ after 45 cycles and then slowly decreased to $310 \text{ mAh}\cdot\text{g}^{-1}$ at the 300th cycle and stabilized. Finally, after 500 cycles, the capacity still reached $285 \text{ mAh}\cdot\text{g}^{-1}$, confirming that NGS1 has excellent cycle stability at high current densities.

Battery contributions, pseudocapacitive contributions and double-layer capacitance contributions composed the integral capacity of the battery. Therefore, discussing the composition of the battery's total capacity helps to further understand the properties. With regard to this, we used the following formulas:

$$i = av^b \quad (1)$$

$$\ln i = b \ln v + \ln a \quad (2)$$

i - the magnitude of electric current,

v - the scanning rate,

a - variables,

b - variables

By calculating the b value with the formula, we could quantify the contribution composition of the capacity. According to previous research, the capacity is mainly the battery contribution when the b value approaches 0.5; when the b value is close to 1, the capacity is mainly the capacitance contribution [58]. Figure 9a shows the CV curve of NGS1 with a scan rate range of 0.2 to $8 \text{ mV}\cdot\text{s}^{-1}$. The values of b are calculated to be 0.65 and 0.85 at a reduction potential of 0.1 V and an oxidation potential of 1.25 V. The linear fit in Figure 9b indicates that the battery capacity at the reduction potential is mainly the battery contribution, which also coincides with the diffusion behaviour of lithium at this potential; at a high potential, the capacitor contribution mainly dominates the battery capacity [59]. Formula 3 can quantitatively analyse the contribution ratio of capacitance to the electrode capacity:

$$i = k_1 v + k_2 v^{1/2} \quad (3)$$

In this formula, $k_1 v$ represents the current of the capacitive behaviour controlled by the surface, and $k_2 v^{1/2}$ is the battery behaviour determined by the redox reaction [60]. Figure 9c shows the linear fit of $i/v^{1/2}$ and $v^{1/2}$ at different voltages, the slope of which is k_1 , and the intercept from the Y axis is k_2 . The resulting capacitance contribution ratio at different potentials is shown in Figure 9d, and the corresponding capacitance contributions are approximately 12%, 15%, 20%, 39%, 41%, 51%, 46%, and 47% from 0.1 to 2.5 V, respectively. After performing multipoint calculations in this way, the capacitive contribution ratio at $0.2 \text{ mV}\cdot\text{s}^{-1}$ can be obtained (Figure 9e). The ratio of the pseudocapacitance contribution integral area is calculated to be 41.4%. A high capacitive contribution is beneficial to the rate stability because capacitive energy storage is characterized by surface control, and lithium ions have difficulty diffusing to the inside of the materials. Thus, the lithiation-delithiation process only occurs on the surface, which results in reduced battery capacity. The capacitive

contribution in the battery can provide additional capacity at high currents, which improves the capacity and stability of the battery at high current densities [61].

The above calculation results showed that the interface engineering of NGs can effectively inhibit the decomposition of cations and electrolytes while also enhancing the conductivity of the electrodes. Interface engineering between the active material and the electrolyte could enhance the structural stability of the electrode. The synergy of NGs in interface engineering and alloying-dealloying reactions can effectively improve the cycling and rate stability of LIBs.

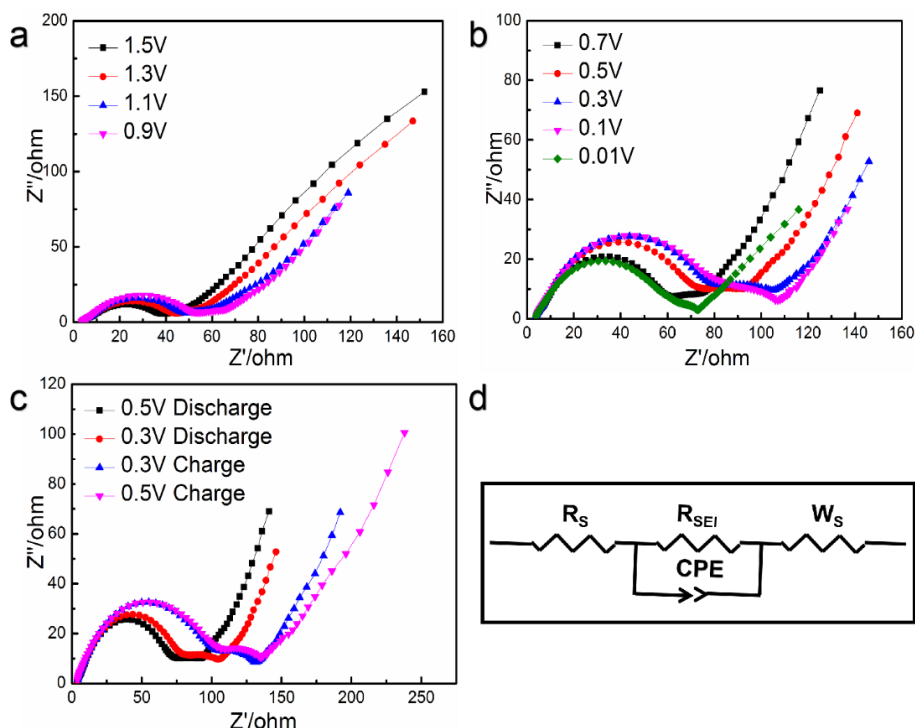


Figure 10. Nyquist plots of the first discharge of NGS1 electrodes at (a) 1.5-0.9 V and (b) 0.7-0.01 V. (c) Nyquist comparison chart of NGS1 electrode charge and discharge in the first cycle at 0.3 V and 0.5 V. (d) The equivalent circuit for the EIS.

Figure 10 shows the AC impedance test (EIS) curve of the NGS1 electrode at different potentials during the first cycle of discharge. The equivalent circuit in Figure 10d includes R_s (charge transfer resistance), R_{SEI} (the resistance of the SEI film) and W_s (Warburg resistance) related to Li^+ diffusion in the electrode [62]. The semicircle in the high-frequency region and the diagonal line in the middle-frequency region form the Nyquist curve, corresponding to R_s and R_{SEI} , respectively [63]. When the potential decreases from 1.5 V to 0.1 V, the R_s gradually increases, which is due to the large amount of charge transfer caused by the lithiation procedure. When the potential drops to 0.01 V, the reduction in R_s is due to the completion of lithium insertion. From Figure 10c, we can observe that the R_s and R_{SEI} of the charging process are much higher than those during the discharging process at the equipotential, which also corresponds to the reduction peak potential in the CV curve and leads to the first lap irreversible capacity.

4. CONCLUSION

NG materials with different nitrogen sources and carbon sources were successfully synthesized by a restricted template method. SEM, TEM, XRD and other characterization methods show that there is no obvious difference in the morphology and structure of the synthesized NG materials, which are formed by stacking graphite layers with curled edges and have considerable numbers of pore structures. The nitrogen doping form of NGs was further analysed by XPS characterization technology, and the relative content of each nitrogen-doped structure was significantly different. When used as anode materials for LIBs, NGs exhibit a high reversible specific capacity and good cycle stability. Among them, NGS1 and NGS2 maintain reversible specific capacities of $780 \text{ mAh}\cdot\text{g}^{-1}$ and $850.7 \text{ mAh}\cdot\text{g}^{-1}$ after 100 cycles, which are higher than those of other NGs. At a current density of $5 \text{ A}\cdot\text{g}^{-1}$, the reversible specific capacity of NGS1 can still reach $331.8 \text{ mAh}\cdot\text{g}^{-1}$, demonstrating its outstanding rate performance. In general, NGs synthesized by the facile reaction steps described exhibit exceptional electrochemical performance and have good development prospects and commercial potential as anodes for lithium-ion batteries.

SUPPORTING INFORMATION

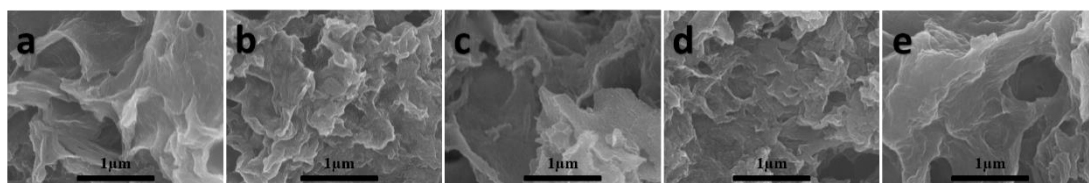


Figure S1 SEM images of (a) NGS1, (b) NGS2, (c) NGS3, (d) NGS4, and (e) NGS5.

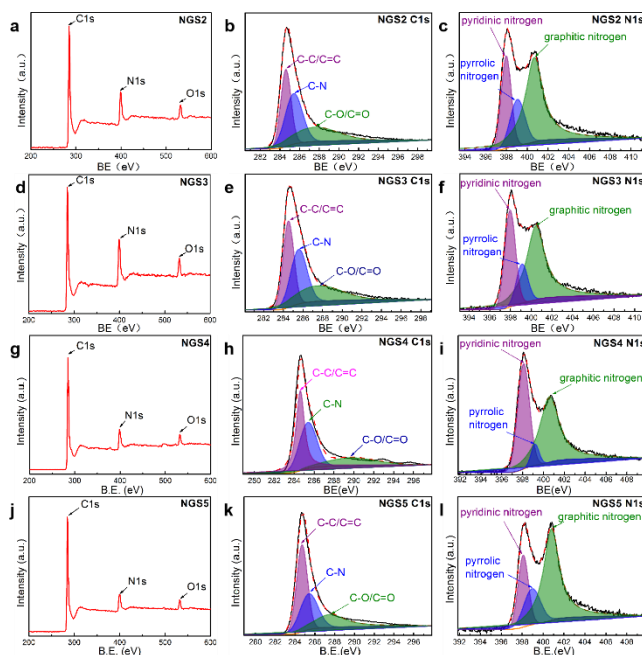


Figure S2 XPS full spectrum, C1s XPS and N1s XPS spectra of NGS2 (a, b, c), NGS3 (d, e, f), NGS4 (g, h, i) and NGS5 (j, k, l).

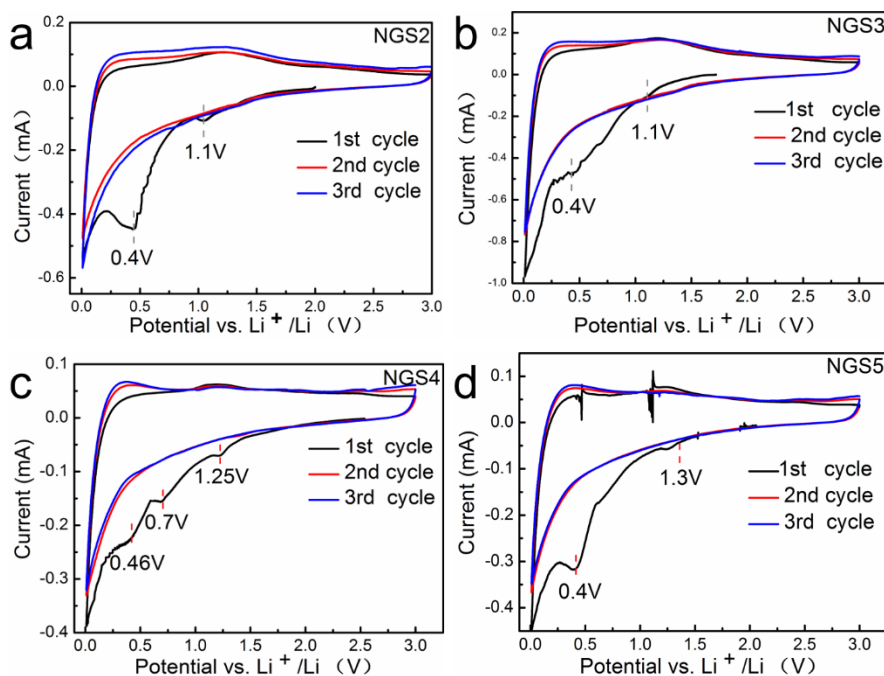


Figure S3 CV curves of (a) NGS2, (b) NGS3, (c) NGS4 and (d) NGS5 at a scan rate of $0.2 \text{ mV}\cdot\text{s}^{-1}$ between 0.01 and 3.0 V versus Li^+/Li .

ACKNOWLEDGEMENTS

This research was supported by the Fundamental Research Funds for the Central Universities (Grant No. 2018BSCXA12) and Postgraduate Research & Practice Innovation Program of Jiangsu Province (Grant No. KYCX18_1931).

References

1. Y.W. Son, M.L. Cohen and S.G. Louie. *Nature*, 444 (2006) 347-349.
2. K.S. Novoselov, A.K. Geim, S.V. Morozov, D. Jiang, Y. Zhang, S.V. Dubonos, I.V. Grigorieva and A.A. Firsov. *Science*, 306 (2004) 666-669.
3. G. Kucinskis, G. Bajars, J. Kleperis. *J. Power Sources*, 240(2013) 66-79.
4. F.L. Zhao, Y. Wang, X. Zhang, X.J. Liang, F. Zhang, L. Wang, Y. Li, Y.Y. Feng and W. Feng. *Carbon*, 161 (2020) 287-298.
5. J. Liu, Y.G. Xu and L.B. Kong. *J. Mater. Sci.: Mater. Electron.*, 31 (2020) 9946-9959.
6. C.P. Mu, X. Du, A.m. Nie, B.C. Wang, F.S. Wen, J.Y. Xiang, K. Zhai, and Z.Y. Liu. *Appl. Phys. Lett.*, 115 (2019) 043103
7. W. Yao, W.J. Qiu, Z.X. Xu, J.G. Xu, J.H. Luo and Y.C. Wen. *Ceram. Int.*, 44 (2018) 21734-21741.
8. N.Z. Zhao, Z.X. Zhao, I.A.D. Williamson, S. Boutami, B. Zhao and S.H. Fan. *ACS Photonics*, 6 (2019) 339-344.
9. Y. Zhang, Y.W. Liu, L. Chen, X.T. Hu, L. Zhang, L. Hu and Y.W. Chen. *RSC Adv.*, 5 (2015) 49614-49622.
10. J.J. Qian, J. Yan, C. Shen, F.N. Xi, X.P. Dong and J.Y. Liu. *J. Mater. Sci.*, 53 (2018) 12103-12114.
11. S. Irvani and R.S. Varma. *Environ. Chem. Lett.*, 18 (2020) 703-727.
12. X.T. Ding, Y.S. Niu, G. Zhang, Y.H. Xu and J.H. Li. *Chem-Asian. J.*, 15 (2020) 1214-1224.
13. Q.W. Liu, J.H. Sun, K. Gao, N. Chen, X.T. Sun, D. Ti, C.C. Bai, R.R. and L.T. Qu. *Mater. Chem. Front.*, 4 (2020) 421-436.

14. T. Maiyalagan, X. Wang, H. Wang. *ACS Catal.*, 2 (2012) 781-794.
15. A. Gomez-Martin, J. Martinez-Fernandez, M. Rutttert, M. Winter, T. Placke, J. Ramirez-Rico. *Carbon*, 164 (2020) 261-271.
16. X.Y. Dong, X. Zheng, Y.C. Deng, L.F. Wang, H.P. Hong, Z.C. Ju. *J. Mater. Sci.*, 55 (2020) 13023-13035.
17. H. Shi, M. Xia, L.T. Jia, B. Hou, Q. Wang and D.B. Li. *Chem. Phys.*, 536 (2020) 110783.
18. H.R. Wang, W.J. Cai, S. Wang, B.Z. Li, Y.G. Yang, Y. Li and Q.H. Wu. *Electrochim. Acta*, 342 (2020) 136107.
19. Q.C. Pan, Y.G. Huang, H.Q. Wang, G.H. Yang, L.C. Wang, J. Chen, Y.H. Zan, Q.Y. Li. *Electrochim. Acta*, 197 (2016) 50-57.
20. P. Lazar, F. Karlicky, P. Jurecka, M. Kocman, E. Otyepkova, K. Safarova, M. Otyepka. *J. Am. Chem. Soc.*, 135 (2013) 6372-6377.
21. B.M. Chong, N.H.N. Azman, M.A.A.M. Abdah, Y. Sulaiman. *Appl. Sci.*, 9 (2019) 1040.
22. Y. Shang, H.Z. Xu, M.Y. Li, G.L. Zhang. *Nano*, 12 (2017) 1750018.
23. B. Zheng. *Mater. Lett.*, 236 (2019) 583-586.
24. Y. An, X. Wei, Z. Yang. *Phys. Chem. Chem. Phys.*, 2012, 14(45):15802-15806.
25. H. Liu, Y. Liu, D. Zhu. *J. Mater. Chem.*, 21 (2011) 3335-3345.
26. L.E. Milagre, V.F. Almeida, S.S. Vieira, T.A. Ribeiro-Santos, M.C. Monteiro de Castro, M.H. Araujo, A.P.C. Teixeira. *Catal. Today*, 344 (2018) 32-40.
27. L. Liu, M. Zhou, L. Jin, L. Li, Y. Mo, G. Su, X. Li, H. Zhu, Y. Tian. *Friction*, 7 (2019) 199-216.
28. L. Qie, W.M. Chen, Z.H. Wang, Q.G. Shao, X. Li, L.X. Yuan, X.L. Hu, W.X. Zhang, Y.H. Huang. *Adv. Mater.*, 24 (2012) 2047-2050.
29. B. Chong, N. Azman, M. Mohd Abdah, Y. Sulaiman. *Appl. Sci.*, 9 (2019) 1040.
30. J. Wang, Z. Yang, Y. Li, X. Fan, S. Wang. *Carbon*, 163 (2020) 43-55.
31. H. Wang, C. Zhang, Z. Liu, W. Li, P. Han, H. Xu, K. Zhang, S. Dong, J. Yao, G. Cui. *J. Mater. Chem.*, 21 (2011) 5430-5434.
32. Y.J. Li, T.C. Xia, T.T. Yu, M. Yang, X.Y. Zhao, L.Q. Ma. *J. Alloys Compd.*, 843 (2020) 156045.
33. H.W. Huang, S.S. Fan, W. Dong, W. Zou, M. Yan, Z. Deng, X. Zheng, J. Liu, H.E. Wang, L. Chen. *Appl. Surf. Sci.*, 473 (2019) 893-901.
34. Q. Chen, R. Zhu, Q. He, S. Liu, D. Wu, H. Fu, J. Du, J. Zhu, H. He. *Chem. Commun.*, 55 (2019) 2644-2647.
35. J.X. Mao, M.M. Chen, Y.C. Deng, H. Liu, Z.C. Ju, Z. Xing, X.C. Cao. *J. Mater. Sci.*, 54 (2019) 12767-12781.
36. Z. Ju, P. Li, G. Ma, Z. Xing, Q. Zhuang, Y. Qian. *Energy Storage Mater.*, 11 (2017) 38-46.
37. M.A.A. Apasiku, A.J.R. Hensley, K. Groden, M. Garcia-Perez, J.S. Mcewen. *Carbon*, 152 (2019) 715-726.
38. S. Pei, H.M. Cheng. *Carbon*, 50 (2012) 3210-3228.
39. S.X. Wang, S.L. Chen, Q.L. Wei, X.K. Zhang, S.Y. Wong, S.H. Sun, X. Li. *Chem. Mater.*, 27 (2015) 336-342.
40. M.P. More, P.K. Deshmukh. *Nanotechnology*, 31 (2020) 432001.
41. A.L.M. Reddy, A. Srivastava, S.R. Gowda, H. Gullapalli, P.M. Ajayan. *ACS Nano*, 4 (2010) 6337-6342.
42. W. Alkarmo, F. Ouhib, A. Aqil, J.M. Thomassin, B. Vertruyen, M.L. Piedboeuf, N. Job, C. Detrembleur, C. Jerome. *J. Mater. Sci.*, 53 (2018) 6135-6146.
43. A. Gomez-Martin, J. Martinez-Fernandez, M. Rutttert, M. Winter, J. Ramirez-Rico. *Carbon*, 164 (2020) 261-271.
44. M. Ayiania, M. Smith, A.J.R. Hensley, L. Scudiero, M. Garcia-Perez. *Carbon*, 162 (2020) 528-544.
45. N.A. Ghany, S. Elsherif, H.T. Handal. *Surf. Interfaces*, 9 (2017) 93-106.
46. L.L. Tian, S.B. Li, M.J. Zhang, S.K. Li, L.P. Lin, J.X. Zheng, Q.C. Zhuang, K. Amine, F. Pan.

- ACS Appl. Mater. Interfaces*, 8 (2016) 26722-26729.
47. Y. Xu, X. Sun, C. Wei, G. Liang. *J. Electroanal. Chem.*, 867 (2020) 114125.
 48. S. Liu, W. Wei, Y. Wang, J. Ren. *Appl. Surf. Sci.*, 485 (2019) 529-535.
 49. J.D. Bagley, D. Kishorekumar, K.A. See, N.C. Yeh. *RSC Adv.*, 10 (2020) 39562-39571.
 50. M.P. Illa, A.D. Pathak, C.S. Sharma, M. Khandelwal. *ACS Appl. Energy Mater.*, 3 (2020) 8676-8687.
 51. Q. Lv, R. Song, B. Wang, H. Zhu, D. Wang. *Ionics*, 26 (2020) 13-22.
 52. Z. Yan, Q.W. Yang, Q. Wang, J. Ma. *Chin. Chem. Lett.*, 31 (2020) 583-588.
 53. D. Lin, Y. Liu, Z. Liang, H.W. Lee, J. Sun, H. Wang, K. Yan, J. Xie, Y. Cui. *Nat. Nanotechnol.*, 11 (2016) 626-632.
 54. S. Sahoo, S. Bae, Y. Lee, J.M. Lee, J.M. Ahn, C.G. Kim, I.K. Oh. *Carbon*, 94 (2015) 455-463.
 55. M. Du, J. Sun, J. Chang, F. Yang, L.J. Shi, L. Gao. *RSC Adv.*, 4 (2014) 42412-42417.
 56. L. Chao, X. Liu, T. Jiang, Q. Wang, W. Hao, C. Zhang. *J. Power Sources*, 342 (2017) 157-164.
 57. X. Li, D. Geng, Z. Yong, X. Meng, R. Li, X. Sun. *Electrochem. Commun.*, 13 (2011) 822-825.
 58. V. Augustyn, J. Come, M.A. Lowe, J.W. Kim, P.L. Taberna, S.H. Tolbert, H.D. AbruA, P. Simon, B. Dunn. *Nat. Mater.*, 12 (2013) 518-522.
 59. E. Raymundo-Pinero, K. Kierzek, J. Machnikowski, F. Beguin. *Carbon*, 44 (2006) 2498-2507.
 60. M. Park, X. Zhang, M. Chung, G.B. Less, A.M. Sastry. *J. Power Sources*, 195 (2010) 7904-7929.
 61. Y. Tao, Z.Y. Sui, B.H. Han. *J. Mater. Chem. A*, 8 (2020) 6125-6143.
 62. Y. Gao, X. Qiu, X. Wang, X. Chen, Z. Yu. *Nanotechnology*, 31 (2019) 155702.
 63. Q. Sun, Y. Huang, S. Wu, Z. Gao, H. Liu, P. Hu, Q. Long. *Nanomaterials*, 9 (2019) 1084.

© 2021 The Authors. Published by ESG (www.electrochemsci.org). This article is an open access article distributed under the terms and conditions of the Creative Commons Attribution license (<http://creativecommons.org/licenses/by/4.0/>).